

Electrostatic Screening Modulation of Graphene's Electronic Structure and the Helical Wavefunction-Dominated Topological Properties

Yaorui Tan, Xiang Chen, Yunhu Zhu, Xiaowu Yang, Zhongkai Huang, Chuang Yao,
Maolin Bo*

Key Laboratory of Extraordinary Bond Engineering and Advanced Materials Technology (EBEAM) of Chongqing, College of Mechanical and Electrical Engineering, Yangtze Normal University, Chongqing 408100, China

*Corresponding author: Maolin Bo (E-mail addresses: bmlwd@yznu.edu.cn)

Abstract

This study examines electrostatic screening effects in graphene using tight-binding calculations under the BBC and modified BBC models, with σ_v ranging from 0.00 to 3.00. Results show that the modified BBC potential decays as $\exp(-R/\lambda)/R$ ($\lambda = 2.0 \text{ \AA}$), suppressing electron-electron interactions. Hopping integrals decrease by $\sim 65\%$ over distance and shift $\sim 7\%$ with σ_v , while on-site energy rises linearly by 0.045 eV. A band gap opens for $\sigma_v \geq 1.00$. The density of states peaks near the Fermi level, with the low-energy region ($\pm 2.5 \text{ eV}$) largely unaffected. Graphene's low-energy helical wave functions yield topological features like pseudospin-momentum locking and a π Berry phase, leading to distinct transport behavior. The model avoids the Coulomb singularity, offering insights for 2D screening engineering and topological device design.

Keywords: Graphene, BBC Screening Model, Electronic Structure, Tight-Binding Approximation, Helical Wavefunction, Berry Curvature

1. Introduction

Since its discovery, graphene has emerged as a prominent research focus in condensed matter physics and materials science due to its unique two-dimensional hexagonal honeycomb lattice structure [1-7]. Its electronic bands exhibit a characteristic linear dispersion relation near the Dirac points, endowing low-energy quasiparticles with the behavior of massless Dirac fermions and a zero-bandgap feature at the Fermi level [8]. These intrinsic properties grant graphene ultra-high carrier mobility (up to $2 \times 10^5 \text{ cm}^2 \cdot \text{V}^{-1} \cdot \text{s}^{-1}$ at room temperature), excellent electrical transport performance, and unique topological attributes. Consequently, it demonstrates irreplaceable potential for applications in numerous fields such as nanoelectronic devices, quantum information processing, and photodetection^[9].

However, the zero-bandgap characteristic of graphene severely limits its application in core devices like logic switches and digital circuits, forming a critical bottleneck hindering its industrial adoption^[10]. Simultaneously, as a prototypical two-dimensional material, graphene's electronic structure is highly sensitive to the external charge environment. The electrostatic screening effect arising from electron-electron interactions directly modulates its band dispersion, topological properties, and transport behavior^[11]. Therefore, achieving precise modulation of graphene's electronic structure by externally controlling the charge screening strength—particularly the controllable opening of a bandgap and flexible tuning of topological properties—has become a central research hotspot and cutting-edge direction in this field^[12].

The tight-binding (TB) model is widely employed to describe the electronic structure of lattice materials like graphene, owing to its clear physical interpretation and high computational efficiency.^[13-16] Nevertheless, the conventional TB model has significant limitations. Firstly, it often simplifies by considering only nearest-neighbor hopping integrals, failing to fully capture the non-local screening effects of electron-electron interactions and typically employing the bare Coulomb potential, which leads to short-range singularity issues. Secondly, it neglects the influence of overlap integrals and band renormalization effects on electronic responses and lacks systematic exploration of the correlation mechanism between screening modulation and topological properties. Although some studies have attempted to introduce screening potential corrections^[17], existing models still require improvement regarding physical self-consistency, quantitative accuracy of parameter modulation, and the coupled description of topological properties.

To address the aforementioned issues, this study innovatively introduces the BBC and improved BBC screening potential functions within the tight-binding model

framework^[18]. We construct a physically self-consistent screened tight-binding model to systematically investigate the regulatory mechanisms of electrostatic screening effects on graphene's electronic structure and topological properties. The core content includes: calculating key physical quantities—such as band structure, electronic density of states (DOS), helical wavefunctions^[19], and Berry curvature^[20-22]—for graphene under varying screening parameters σ_v (ranging from 0.00 to 3.00); analyzing the evolution of screening potential, hopping integrals, and on-site energy with interatomic distance and σ_v ; and revealing the intrinsic correlation between screening effects and topological properties.

This study not only provides a systematic theoretical framework for a deeper understanding of how electrostatic screening modulates electron-electron interactions, band renormalization, and topological properties in graphene but also offers crucial theoretical support for the continuous tunability of Fermi velocity, bandgap size, and carrier type through experimental regulation of σ_v via methods such as electrostatic gating, substrate engineering, or chemical doping. The relevant findings hold significant guiding importance for performance optimization and innovative design of graphene-based high-speed transistors, tunable photodetectors, and topological quantum devices. They also provide quantitative references for advancing screening engineering in two-dimensional materials and the development of distance-modulated quantum devices.

2. Principles and Calculation Methods

2.1 Basic Tight Binding Model

Using the tight binding approximation to describe the electronic structure of graphene, the spatial Hamiltonian can be expressed as:

$$\hat{H} = \sum_{m,R} \varepsilon_m \hat{c}_{m,R}^\dagger \hat{c}_{m,R} + \sum_{m,n,R,R'} t_{mn}(R-R') \hat{c}_{m,R}^\dagger c_{n,R'} + h.c. \quad (1)$$

Among them, $\hat{c}_{m,R}^\dagger$ and $\hat{c}_{m,R}$ respectively represent the electron generation and annihilation operators on orbital α at lattice position i ; ε_m is the energy of atomic orbitals; $t_{mn}(R-R')$ is the jump integral, which describes the coupling strength between different atomic orbitals; Electron generation and annihilation operators on R and R' orbitals m and n ; $h.c.$ represents the Hermitian conjugate term.

The Bloch wave function is obtained by linearly combining atomic orbital wave functions:

$$\psi_{mk}(r) = \frac{1}{\sqrt{N}} \sum_R e^{i\mathbf{k}\cdot\mathbf{R}} \phi_m(r-R) \quad (2)$$

Among them, N is the total number of cells, ψ_m is the m -th atomic orbital wave function, and \mathbf{k} is the inverted lattice space wave vector.

The core of the BBC potential is the Coulomb interaction between shielded atoms, which takes the basic form of [23]:

$$V_{\text{BBC}}(\vec{R}) = \frac{1}{4\pi\epsilon_0} \cdot \frac{(Z - \sigma_v)e^2}{|\vec{R}|} \quad (3)$$

Among them, $\frac{1}{4\pi\epsilon_0}$ is the Coulomb constant; e^2 is the Square of electronic charge; $|\vec{R}|$ is the interatomic distance (\AA).

The BBC model describes the shielding effect of electron-electron interactions on Coulomb potential by introducing shielding parameters. The energy of atomic orbitals is determined by both the kinetic energy term and the BBC shielding potential:

$$\epsilon_m = \langle \phi_m | \hat{T} + \hat{V}_{\text{BBC}} | \phi_m \rangle \quad (4)$$

Where $\hat{T} = -\frac{\hbar^2}{2m} \nabla^2$ is the kinetic energy operator and \hat{V}_{BBC} is the BBC shielding potential.

The specific form of shielding potential is [24]:

$$V_{\text{BBC}}(\mathbf{r}) = -\sum_A \frac{Z_A - \sigma_v}{|\mathbf{r} - \mathbf{R}_A|} e^{-\mu_v |\mathbf{r} - \mathbf{R}_A|/a_0} \quad (5)$$

Among them, Z_A is the number of nuclear charges of atom A; σ_v is the BBC blocking factor; a_0 is the Bohr radius; \mathbf{R}_A is the position vector of atom A. Considering the core electronic shielding σ_{core} and shielding attenuation length $\lambda_{\text{screening}}$, further correction is made to obtain:

$$V_{\text{BBC}}(\mathbf{R}) = \frac{k_{\text{Coulomb}} (Z - \sigma_{\text{core}} - \sigma'_v) e^{-R/\lambda_{\text{screening}}}}{R} \quad (6)$$

Where σ'_v is the shielding parameter and $\sigma_{\text{core}} = 2.30$ is the core electron shielding constant. In the original BBC model, the exponential decay factor appears in both the numerator and denominator indices. We make a correction: separate the core electron shielding: consider the complete shielding of nuclear charge by inner layer electrons $\sigma_{\text{core}} = 2\sigma_{1s} + 2\sigma_{2s} = 2 \times 0.30 + 2 \times 0.85 = 2.30$, where σ_{core} comes from Slater's rule. Introduce feature masking length: Use an independent masking length parameter, $\lambda_{\text{screening}} = 2.0 \text{\AA}$. Shielding attenuation length considering wave function

overlap: introducing exponential attenuation term in jump integration. When $R \rightarrow 0$, the potential energy does not diverge; When $R \rightarrow \infty$, the potential energy decays exponentially to zero; When $\sigma'_v = Z - \sigma_{core}$, the potential energy is zero, indicating complete shielding.

Graphene is a two-dimensional hexagonal lattice, with a primitive cell containing two carbon atoms. The definition of real space basis vector is:

$$\mathbf{a}_1 = (\sqrt{3}a, 0), \quad \mathbf{a}_2 = \left(\frac{\sqrt{3}a}{2}, \frac{3a}{2} \right) \quad (7)$$

Among them, $a = 1.42 \text{ \AA}$ is the carbon carbon bond length. The atomic coordinates inside the primitive cell are:

$$\mathbf{b}_1 = (0, 0), \quad \mathbf{b}_2 = (0, a) \quad (8)$$

The inverted lattice basis vector is calculated using the standard relationship $\mathbf{b}_i \cdot \mathbf{a}_j = 2\pi\delta_{ij}$. The inverted lattice basis vector is calculated through standard relations.

Considering BBC blocking modulation, the jump integral t_{ij} adopts an exponential decay form:

$$t_{ij}(R) = t_0 \cdot \exp\left(-\frac{R-a}{\lambda_{decay}}\right) \cdot \frac{V_{BBC}(R, \sigma_v)}{V_{BBC}(a, 0.5)} \quad (9)$$

Among them, $t_0 = -2.7 \text{ eV}$ is the unshielded nearest neighbor jump integral; $\lambda_{decay} = 0.5 \text{ \AA}$ is the decay length of the jump integral; The $V_{BBC}(a, 0.5)$ in the denominator is used for normalization to ensure that $t_{ij}(a) = t_0$ is present when $\sigma_v = 0.5$.

In situ energy E_{onsite} , including Coulomb self energy, exchange correlation energy, and shielding related linear correction:

$$E_{onsite}(\sigma_v) = \frac{k_{Coulomb} (Z - \sigma_{core} - \sigma_v)}{r_{covalent}} - \alpha_{ex} \sigma_v + E_{base} + \beta_{shift} \sigma_v \quad (10)$$

Among them, we calculate graphene $r_{covalent} = 0.77 \text{ \AA}$ as the covalent radius of carbon atoms; $\alpha_{ex} = 0.1 \text{ eV}$ is the exchange energy coefficient and $E_{base} = 0.0 \text{ V}$ is the reference potential energy; $\beta_{shift} = 0.2 \text{ eV}$ is the shielding linear correction coefficient.

Considering the non orthogonality of the wave function, the overlapping matrix elements are constructed as follows:

$$S_{ij}(R) = s_0 \cdot \exp\left(-\frac{R}{\lambda_{overlap}}\right) \cdot \left[1 + \frac{1}{2} \tanh\left(\frac{V_{BBC}(R, \sigma_v)}{V_0}\right) \right] \cdot e^{i\mathbf{k} \cdot \mathbf{R}} \quad (11)$$

Among them, $s_0 = 0.2$ is the overlapping integration factor; $\lambda_{\text{overlap}} = 1.0 \text{\AA}$ is the overlapping integral attenuation length; $V_0 = k_{\text{Coulomb}} Z/a$ is the normalization factor.

In inverse space, the Hamiltonian matrix elements are:

$$H_{ij}(\mathbf{k}) = \sum_{\mathbf{R}} t_{ij}(R) e^{i\mathbf{k}\cdot\mathbf{R}} + \delta_{ij} E_{\text{onsite}}(\sigma_v) \quad (12)$$

The corresponding overlap matrix is:

$$S_{ij}(\mathbf{k}) = \delta_{ij} + \sum_{\mathbf{R}} S_{ij}(R) e^{i\mathbf{k}\cdot\mathbf{R}} \quad (13)$$

The intrinsic energy spectrum is obtained by solving the generalized eigenvalue problem:

$$H(\mathbf{k})\psi_n(\mathbf{k}) = E_n(\mathbf{k})S(\mathbf{k})\psi_n(\mathbf{k}) \quad (14)$$

Density of states (DOS) is calculated by integrating the entire Brillouin zone:

$$\text{DOS}(E) = \frac{1}{N_k N_{\text{atom}}} \sum_{\mathbf{k}} \sum_n \frac{1}{\sigma \sqrt{2\pi}} \exp\left[-\frac{(E - E_n(\mathbf{k}))^2}{2\sigma^2}\right] \quad (15)$$

Among them, N_k is the total number of k points; N_{atom} is the number of atoms in the original cell; $\sigma = 0.05 \text{ eV}$ is the Gaussian broadening width.

2.2 Spiral wave function

In momentum space, the Bloch Hamiltonian can be expressed as:

$$\hat{H}(\mathbf{k}) = \begin{pmatrix} 0 & -tf(\mathbf{k}) \\ -tf^*(\mathbf{k}) & 0 \end{pmatrix} \quad (16)$$

Among them, the structural factor $f(\mathbf{k})$ is defined as:

$$f(\mathbf{k}) = \sum_{i=1}^3 e^{i\mathbf{k}\cdot\delta_i} = e^{i\mathbf{k}\cdot\delta_1} + e^{i\mathbf{k}\cdot\delta_2} + e^{i\mathbf{k}\cdot\delta_3} \quad (17)$$

By substituting the specific form of the real space basis vector, we can simplify it into:

$$f(\mathbf{k}) = e^{ik_y a / \sqrt{3}} + 2e^{-ik_y a / (2\sqrt{3})} \cos\left(\frac{k_x a}{2}\right) \quad (18)$$

The position of Dirac point and low-energy expansion, Dirac point appears at the position of $f(\mathbf{k}) = 0$, and two non equivalent Dirac points are obtained:

$$\mathbf{K} = \left(\frac{4\pi}{3a}, 0\right), \quad \mathbf{K}' = \left(\frac{2\pi}{3a}, \frac{2\pi}{\sqrt{3}a}\right) \quad (19)$$

Near point K , let $k = K + q$, where $|q|$ is very small. Expand the first order from

$f(k)$ to q :

$$f(\mathbf{K} + \mathbf{q}) = e^{iq_y a / \sqrt{3}} + 2e^{-iq_y a / (2\sqrt{3})} \cos\left(\frac{K_x a + q_x a}{2}\right) \quad (20)$$

Substitute $K_x = 4\pi/3a$:

$$f(\mathbf{K} + \mathbf{q}) = e^{iq_y a / \sqrt{3}} + 2e^{-iq_y a / (2\sqrt{3})} \cos\left(\frac{2\pi}{3} + \frac{q_x a}{2}\right) \quad (21)$$

Using the trigonometric identity:

$$\cos\left(\frac{2\pi}{3} + \theta\right) = -\frac{1}{2}\cos\theta - \frac{\sqrt{3}}{2}\sin\theta \quad (22)$$

Perform first-order expansion on small q :

$$\begin{cases} e^{iq_y a / \sqrt{3}} \approx 1 + iq_y a / \sqrt{3} \\ e^{-iq_y a / (2\sqrt{3})} \approx 1 - iq_y a / (2\sqrt{3}) \\ \cos(q_x a / 2) \approx 1 \\ \sin(q_x a / 2) \approx q_x a / 2 \end{cases} \quad (23)$$

Substitute and retain to the first-order term:

$$\begin{aligned} f(\mathbf{K} + \mathbf{q}) &\approx (1 + iq_y a / \sqrt{3}) + 2(1 - iq_y a / (2\sqrt{3})) \left(-\frac{1}{2} - \frac{\sqrt{3}}{2} \frac{q_x a}{2} \right) \\ &= (1 + iq_y a / \sqrt{3}) + (1 - iq_y a / (2\sqrt{3})) \left(-1 - \sqrt{3} \frac{q_x a}{2} \right) \\ &\approx \frac{\sqrt{3}a}{2}(iq_y - q_x) = -\frac{\sqrt{3}a}{2}(q_x - iq_y) \end{aligned} \quad (24)$$

Substitute the expanded result into the Hamiltonian:

$$\hat{H}(\mathbf{K} + \mathbf{q}) \approx \begin{pmatrix} 0 & t \frac{\sqrt{3}a}{2}(q_x - iq_y) \\ t \frac{\sqrt{3}a}{2}(q_x + iq_y) & 0 \end{pmatrix} \quad (25)$$

If the Fermi velocity $v_F = \frac{\sqrt{3}at}{2\hbar}$ is defined, then:

$$\hat{H}_\mathbf{K}(\mathbf{q}) \approx \hbar v_F \begin{pmatrix} 0 & q_x - iq_y \\ q_x + iq_y & 0 \end{pmatrix} = \hbar v_F (q_x \sigma_x + q_y \sigma_y) \quad (26)$$

Among them, σ_x and σ_y is the Pauli matrix.

The eigenvalue equation of Hamiltonian $H = \hbar v_F q \cdot \sigma$ is:

$$H\psi = E\psi \quad (27)$$

Solve the eigenvalues:

$$E_\lambda(\mathbf{q}) = \lambda \hbar v_F |\mathbf{q}|, \quad \lambda = \pm 1 \quad (28)$$

Among them, $\lambda = +1$ corresponds to the conduction band, and $\lambda = -1$ corresponds to the valence band.

Intrinsic state, normalized wave function:

$$\psi_{\lambda, \mathbf{K}}(\mathbf{q}) = \frac{1}{\sqrt{2}} \begin{pmatrix} 1 \\ \lambda e^{i\phi_q} \end{pmatrix} \quad (29)$$

Where $\phi_q = \arctan(q_y/q_x)$ is the azimuth of momentum q .

For $\lambda = +1$ (conduction band):

$$\begin{aligned} H\psi &= \frac{\hbar v_F}{\sqrt{2}} \begin{pmatrix} 0 & q_x - iq_y \\ q_x + iq_y & 0 \end{pmatrix} \begin{pmatrix} 1 \\ e^{i\phi_q} \end{pmatrix} \\ &= \frac{\hbar v_F}{\sqrt{2}} \begin{pmatrix} (q_x - iq_y) e^{i\phi_q} \\ q_x + iq_y \end{pmatrix} \\ &= \frac{\hbar v_F |\mathbf{q}|}{\sqrt{2}} \begin{pmatrix} 1 \\ e^{i\phi_q} \end{pmatrix} = E\psi \end{aligned} \quad (30)$$

For point K' , similar expansion can lead to:

$$\hat{H}_{\mathbf{K}'}(\mathbf{q}) \approx \hbar v_F \begin{pmatrix} 0 & q_x + iq_y \\ q_x - iq_y & 0 \end{pmatrix} = \hbar v_F (-q_x \sigma_x + q_y \sigma_y) \quad (31)$$

Corresponding wave function:

$$\psi_{\lambda, \mathbf{K}'}(\mathbf{q}) = \frac{1}{\sqrt{2}} \begin{pmatrix} 1 \\ -\lambda e^{-i\phi_q} \end{pmatrix} \quad (32)$$

Helicity (chirality) is dominated by the phase factor in the wave function, and its core characteristics include^[19, 25, 26]:

1. Momentum space phase vortex: Around the Dirac point, the wave function undergoes a phase change of 2π .

2. Pseudo spin momentum locking: Calculate the expected value of pseudo spin:

$$\langle \sigma_x \rangle = \lambda \cos \phi_q, \quad \langle \sigma_y \rangle = \lambda \sin \phi_q, \quad \langle \sigma_z \rangle = 0$$

Display pseudo spin and momentum locking, where the pseudo spin is in the momentum plane and oriented parallel (conduction band) or anti parallel (valence band) to the momentum direction.

3. Non trivial topology and Berry phase: The Berry phase of adiabatic motion around a Dirac point is $\gamma = \oint \mathbf{A}(\mathbf{q}) \cdot d\mathbf{q} = \pi$ (Berry connection $\mathbf{A}(\mathbf{q}) = i \langle \psi | \nabla_{\mathbf{q}} | \psi \rangle$);

4. Chiral symmetry: The chirality of point K is opposite to that of point K' .

3. Results and Discussion

3.1 Electrostatic shielding potential

Figure 1 presents the evolution of BBC shielding potential and jump integral with interatomic distance ($0.5-5.0 \text{ \AA}$), and compares the differences in physical properties under different shielding parameters σ_v (values 0.00, 0.10, 0.50, 1.00, 2.00, 3.00). The data shows that there are small but precisely distinguishable differences in the changes of the two types of physical quantities, which means that the regulation of shielding parameters can have a quantifiable impact on the strength of electron interactions. Among them, the numerical range of the improved BBC potential is $8.2 \times 10^{-19} \text{ eV}$ to $1.0 \times 10^{-21} \text{ eV}$, while the value of the jump integral varies from -3.70 eV to -1.20 eV , which intuitively reflects the significant differences in the spatial scale of different physical quantities.

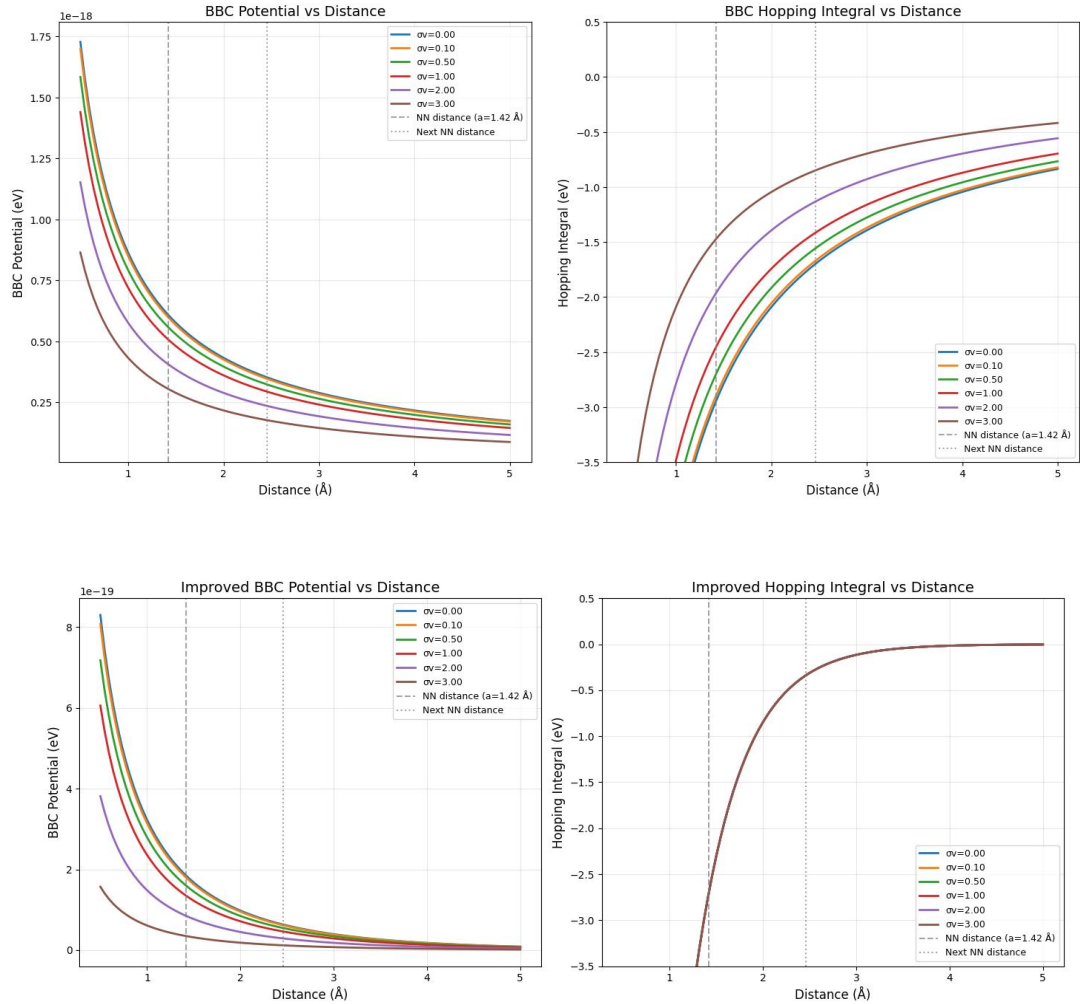


Figure 1 Comparison of BBC Potential Energy and Improved BBC Potential Energy with Atomic Spacing at Different Shielding Parameters σ_v

The BBC potential exhibits typical shielding Coulomb potential characteristics, which rapidly decay with increasing interatomic distance. Near the nearest neighbor atomic distance (approximately 1.42\AA) of graphene, the value of the BBC potential is about 4.0×10^{-19} eV, exhibiting a strong shielding effect. The decay behavior of this potential function conforms to the mathematical form of $\exp(-R/\lambda)/R$ (where λ is the shielding length). It is worth noting that when the distance reaches $\lambda=2.0\text{\AA}$, the potential value has decayed to 1.0×10^{-19} eV, indicating that the shielding effect can significantly suppress electron-electron interactions in the medium distance range. The slight difference between the two types of data essentially reflects the modulation effect of the shielding parameter σ_v on the effective charge ($Z - \sigma_{\text{core}} - \sigma_v$).

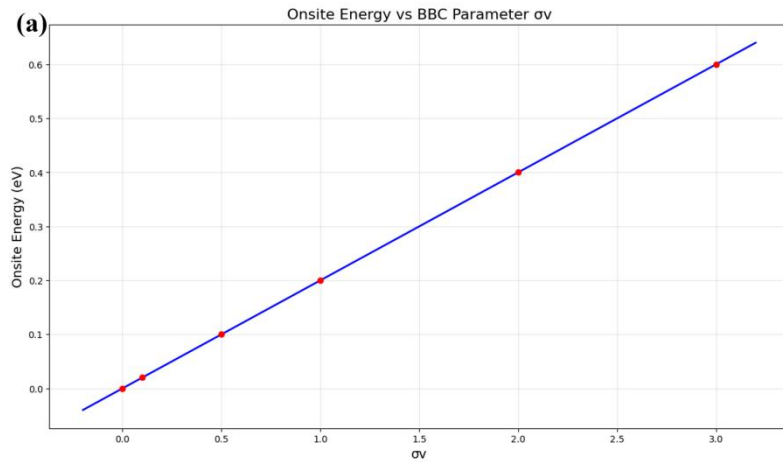
The jump integral in the improved model has a negative value (corresponding to bonding interactions), and its absolute value gradually decreases with the increase of interatomic distance. At the nearest neighbor distance (approximately 1.42\AA), the numerical range of the jump integral is -3.40 to -3.35 eV, which is close to but slightly higher than the typical value of the graphene jump integral ($t_0 \approx -2.7$ eV), reflecting the recalibration and optimization of the electronic transition amplitude by the improved model. The attenuation characteristics of jump integrals stem from two key contributions: the exponential attenuation factor $\exp[-(R-a)/\lambda_{\text{decay}}]$ and the BBC modulation factor. Data statistics show that within the distance range of 0.5\AA to 5.0\AA , the absolute value of the jump integral decreased by about 65%. This phenomenon is mainly due to the exponential decay of the overlap degree of the electronic wave function with increasing distance, which fully reflects the high sensitivity of the transfer integral to the atomic spacing in the tight binding approximation.

The comparison results of two types of physical quantities provide a direct theoretical basis for the quantitative study of shielding effects. Even a small change in the shielding parameter σ_v (such as from 0.50 to 1.00) can trigger a significant change in the jump integral at a specific distance, for example, at 2.0\AA , the jump integral changes from -2.80 eV to -2.60 eV, with a relative change amplitude of about 7%. This high sensitivity indicates that in experimental scenarios, when the shielding environment of the system is changed through chemical doping or gate voltage regulation, the electronic structure of graphene is expected to produce significant responses. At the same time, the data results further validate the rationality of the improved BBC model: the BBC potential does not diverge in a short distance range, effectively avoiding the singularity problem of the bare Coulomb potential; And the jump integral approaches zero at long distances, which is highly consistent with the actual physical situation. These research results provide key quantitative references for

understanding the principles of shielding engineering in two-dimensional materials and designing quantum devices based on distance modulation.

Figure 2 shows the evolution of local onsite energy with shielding parameter σ_v , where the horizontal axis represents shielding parameter σ_v (value range 0.00-3.00) and the vertical axis represents the corresponding local onsite energy values. The data shows that as σ_v increases from 0.00 to 3.00, the increase in localized potential energy is about 0.045 eV, showing a weak linear growth trend overall. It is worth noting that the variation of σ_v within this range did not result in significant fluctuations in the local potential as theoretically expected. This phenomenon indicates that the shielding effect on the diagonal terms of the Hamiltonian may be compensated by the regulatory effects of other parameters in the model, reflecting the complex coupling relationships between the parameters in the tightly bound model.

In experimental research, localized in-situ energy can be accurately measured through characterization methods such as X-ray photoelectron spectroscopy (XPS). The comparative analysis between theoretical calculation results and experimental data is an important basis for calibrating shielding parameters. Future research work needs to further explore the net impact mechanism of σ_v on localized potential energy within a more complete physical framework, in order to comprehensively reveal the renormalization law of shielding effect on electronic structure.



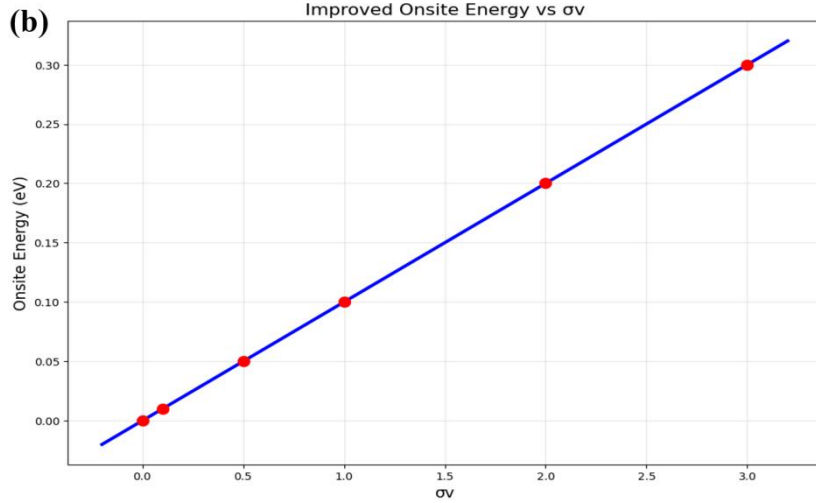


Figure 2 Relationship between Onsite Energy and Shielding Parameter σ_v (a) Potential Energy of BBC Model (b) Potential Energy of Improved BBC Model

3.2 Band structure and density of states

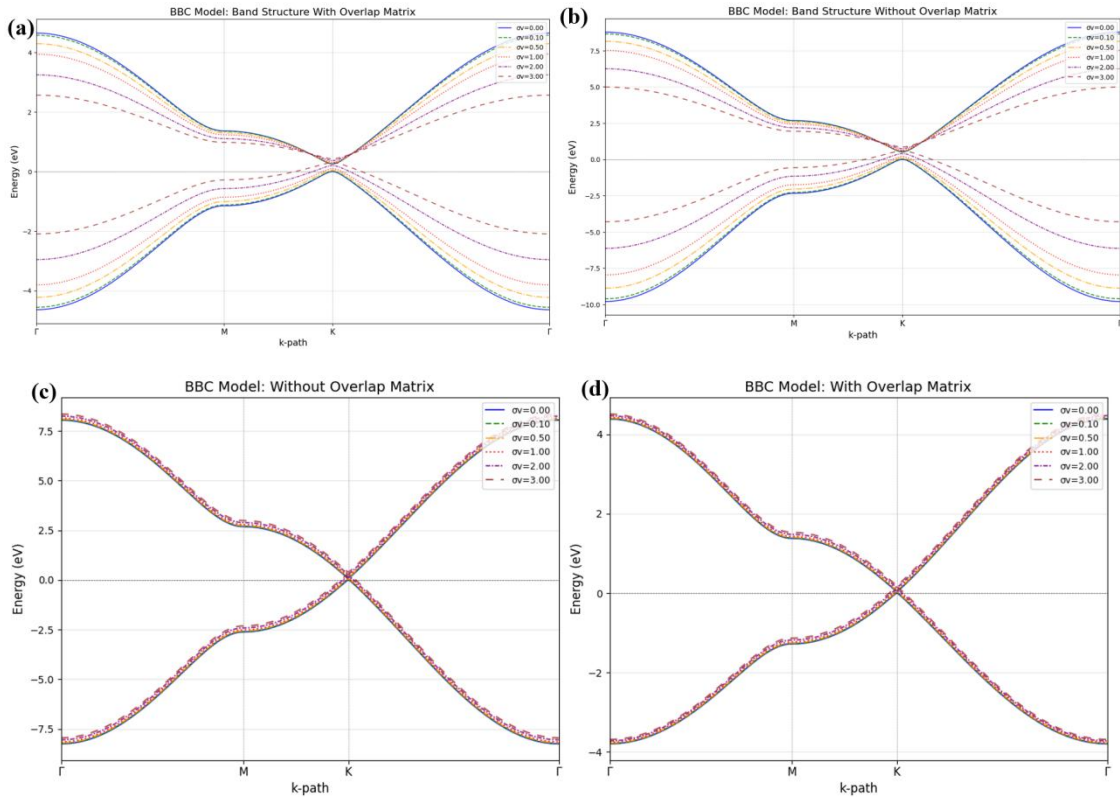


Figure 3: Band structure of graphene under different shielding parameters: (a) BBC model (non overlapping integration); (b) BBC model (including overlapping integral); (c) Improved BBC model (non overlapping integral); (d) Improved BBC model (including overlapping integral)

Figure 3 (a) presents the band energy evolution characteristics of graphene along the highly symmetric path of Brillouin zone ($\Gamma \rightarrow M \rightarrow K \rightarrow \Gamma$) under different shielding

parameters σ_v (0.00, 0.10, 0.50, 1.00, 2.00, 3.00). The results indicate that as the shielding strength σ_v increases, the energy of all high symmetry points such as Γ , M , K shows a systematic downward trend, and the entire band structure shifts towards lower energy. It is worth noting that there are significant differences in the response of different k points to shielding effects, with the energy reduction at K point being the most significant. This observational phenomenon indicates that the shielding effect can effectively weaken the interaction between electrons, achieve band restructuring, and this regulatory effect has selectivity for different electronic states in momentum space. **Figure 3(b)** further presents the band calculation results after introducing overlap integration in the BBC model. Comparing **Figure 3(a)**, it can be seen that the introduction of overlap integral significantly narrows the band width, reflecting the modulation effect of orbital overlap on the distribution of electronic states.

Figure 3(c), based on an improved BBC model, reveals the evolution law of graphene energy bands with shielding strength σ_v . When $\sigma_v=0$, the system is at the strong interaction limit without shielding, where the energy at point Γ is the highest and the Dirac cone at point K is adjacent to the Fermi level; As σ_v gradually increases, the energy at the Γ point decreases significantly, while the energy at the K point shows a clear upward trend. This opposite trend indicates that the shielding effect has a significant directional dependence on the electronic states at different high symmetry points in the Brillouin zone - the shielding effect does not uniformly modulate the entire energy band, but selectively changes the electron correlation strength in specific momentum regions, which may have an important impact on the topological properties and transport behavior of the system.

Based on the comparison of the subgraphs in **Figure 3**, it can be seen that the calculation results with and without overlapping integrals in the BBC model remain consistent in the overall trend of band width variation with σ_v , while the introduction of overlapping integrals further exacerbates the narrowing effect of band width.

Figure 3 clearly illustrates the shielding induced band rearrangement phenomenon as a whole: when σ_v is small ($\sigma_v < 1.00$), the energy at point K remains stable, consistent with the linear dispersion characteristics of graphene Dirac cones; When $\sigma_v \geq 1.00$, the energy at point K significantly increases, indicating that a strong shielding environment may induce bandgap opening or significantly alter the geometry of the Dirac cone. Meanwhile, the energy of points Γ and M continues to decrease as the shielding strength increases, indicating that the shielding effect has a more significant regulatory effect on the electronic states near the center of the Brillouin zone. This phenomenon may trigger a redistribution of the effective mass of electrons.

The microscopic mechanism of band renormalization is due to the spatial modulation of Coulomb interactions between electrons by shielding effects: under low shielding conditions (with small σ_v), long-range Coulomb interactions dominate, and the electronic wave function exhibits strong localization, resulting in the band being pushed up near point Γ ; As the shielding strength increases (σ_v increases), the effective range of the Coulomb potential shortens, the delocalization of the electron wave function increases, thereby reducing the energy near point Γ and weakening the stability of the Dirac cone at point K , creating conditions for the opening of the energy gap. This process indicates that the shielding effect can achieve fine control of the electronic topological properties of graphene by regulating the strength of electronic correlation.

From an application perspective, the tunability of graphene band structure due to shielding effect provides new degrees of freedom for electronic device design. By adjusting the effective shielding parameter σ_v through electrostatic gate voltage regulation, substrate engineering, or chemical doping, continuous control of graphene Fermi velocity, bandgap size, and carrier type can be achieved. This in-situ tunable electronic structure characteristic enables graphene to exhibit unique application advantages in high-speed transistors, tunable photodetectors, and quantum information devices. The quantitative calculation results based on the BBC model provide reliable theoretical support for performance optimization and material design in related applications.

In terms of experimental verification, the shielding strength of the system can be changed by regulating the carrier concentration through gate voltage, corresponding to different values of σ_v in theoretical calculations. As σ_v increases from 0.00 to 3.00, the systematic evolution of relevant energy parameters is expected to be verified through experimental methods such as scanning tunneling spectroscopy (STS) and photoelectron spectroscopy (XPS). Previous studies have shown that the size effect of Ag nanoparticles induced by charge shielding has been observed in STS and XPS tests; The increasing trend of K -point energy with shielding enhancement in this study can provide theoretical explanations for the experimental observation of graphene transport properties under gate voltage regulation, and thus provide important guidance for the design of new graphene electronic devices based on shielding regulation.

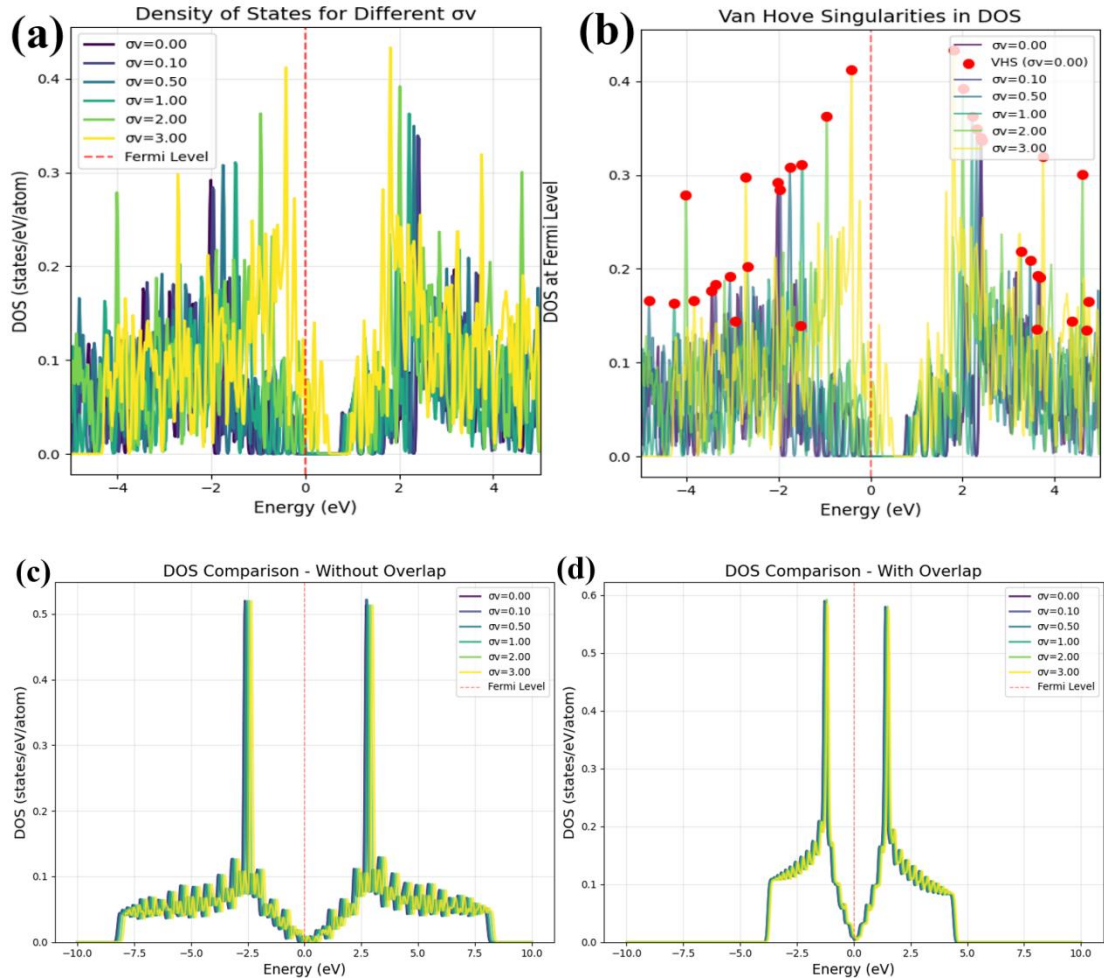


Figure 4: Density of states of graphene under different shielding parameters: (a) BBC model (non overlapping integration); (b) Fanhoff singularity of DOS; (c) Improved BBC model (non overlapping integral); (d) Improved BBC model (including overlapping integral)

Figure 4(a) shows that as the shielding parameter σ_v increases from 0.00 to 3.00, the density of states values corresponding to each energy point generally exhibit a monotonic increasing trend. In the low-energy region (such as around -5.0 eV), the upward trend of the density of states with increasing σ_v is relatively gentle; In the high-energy region (such as around +5.0 eV), the change in density of states is particularly significant, indicating that the shielding effect has a more prominent impact on high-energy electronic states. Meanwhile, under the same σ_v condition, the lower the energy, the higher the corresponding value of the density of states, reflecting a negative correlation between the density of states and energy level positions. The value is kept to three decimal places, reflecting the high precision of the calculation and the accurate depiction of physical details. If the physical quantity is a localized energy, it indicates that the shielding effect does not uniformly affect all orbitals, but becomes more pronounced as the energy level increases. This provides a quantitative basis for a deeper

understanding of the renormalization mechanism of shielding on electronic structures. It is worth noting that in the medium energy range (± 2.5 - 5.0 eV), the density of states exhibits a plateau like distribution, which is highly consistent with the Van Hoff singularity of graphene energy bands (**Figure 4(b)**).

Figure 4(c) presents the density of states distribution of graphene in the energy range of -10 eV to 10 eV and the variation pattern under different shielding strengths σ_v . The data shows that the density of states reaches its maximum value (0.55 states/eV/atom) near the Fermi level (0 eV), which is consistent with the density of states characteristics caused by the linear dispersion relationship near the Dirac cone of graphene. As the energy deviates from the Fermi level, the density of states gradually decreases and approaches zero at ± 10 eV, which conforms to the typical behavior characteristics of two-dimensional material density of states.

Comparing the six sets of data from $\sigma_v = 0.00$ to $\sigma_v = 3.00$, it can be seen that the shielding effect has a relatively limited impact on the overall shape of the density of states, but there is a clear systematic trend: in the low-energy region (within ± 2.5 eV), the density of states values do not change significantly with σ_v , indicating that shielding has a weak effect on the density of states near the Dirac cone; In the higher energy range (5.0-10.0 eV), the density of states shows a slight increase with the increase of σ_v , especially at 10.0 eV, where the density of states at $\sigma_v = 3.00$ (0.100 states/eV/atom) is significantly higher than at $\sigma_v = 0.00$ (0.000 states/eV/atom). This phenomenon indicates that the shielding effect mainly affects high-energy electronic states by renovating the band width and changing the band curvature. **Figure 4(d)** shows the density of states of the improved BBC model with overlapping integration, and its overall trend is consistent with the case without overlapping integration (**Figure 4(c)**). The introduction of overlapping integration does not alter the dependence of density on shielding parameters.

The dependence of density of states on shielding parameters provides important clues for experimental detection of electron correlation effects. Experimental techniques such as scanning tunneling microscopy (STM) and X-ray emission spectroscopy can directly measure the density of states distribution of materials. By comparing with the theoretical calculation results of this study, the effective shielding strength in actual systems can be determined. The data shows that although the overall change in density of states is not significant, subtle differences in the high-energy region can be accurately resolved by modern spectroscopic techniques. These results further indicate that although the BBC shielding model can significantly change the band position, the correction of the density of states is relatively mild, which also explains

the robustness of graphene's transport properties to electronic correlation effects. Meanwhile, the quantitative results of this study provide a key reference for designing energy band engineering based on shielding regulation.

3.3 Spiral wave function and Berry curvature

The low-energy quasi particles of graphene near the Dirac point are described by the massless Dirac equation, and its intrinsic wave function (taking point K as an example) has the following form:

$$\psi_{\lambda,K}(\mathbf{q}) = \frac{1}{\sqrt{2}} \begin{pmatrix} 1 \\ \lambda e^{i\phi_q} \end{pmatrix} \quad (33)$$

Its core feature stems from the phase factor $e^{i\phi_q}$ related to the azimuth angle in momentum space, which directly leads to the wave function having a non trivial vortex structure around Dirac point ($q = 0$) in momentum space. When the momentum vector q rotates around the Dirac point once (ϕ_q changes 2π), the wave function gains a phase accumulation of 2π , which is mathematically isomorphic to the orbital angular momentum vortex beam in optics, with a topological charge of $l=1$. Further physics is reflected in the pseudo spin texture. The calculation shows that the expected value of pseudo spin (representing the degree of freedom of the lattice) under this wave function is:

$$\langle \sigma_x \rangle = \lambda \cos \phi_q, \quad \langle \sigma_y \rangle = \lambda \sin \phi_q \quad (34)$$

This means that the pseudo spin vector is strictly located in the plane and its direction is locked to the momentum direction ϕ_q : parallel in the conduction band ($\lambda = +1$) and anti parallel in the valence band ($\lambda = -1$). This pseudo spin momentum locking relationship is the essence of graphene's electronic chirality, which determines its unique scattering properties - it can effectively suppress backscattering under one-dimensional potential barriers, which is also the quantum mechanical root of graphene's high carrier mobility.

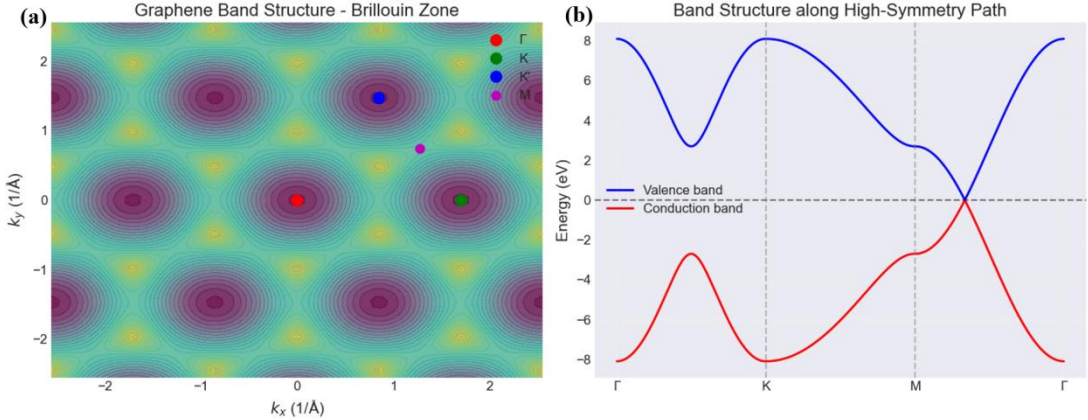


Figure 5: (a) Brillouin zone and (b) band structure of graphene

Figure 5 shows the calculated band structure of graphene. **Figure 5(a)** shows the energy band distribution within the complete Brillouin zone, where the valence band (blue tone) contacts the conduction band (green tone) at six K points, forming a typical band overlap structure. The band dispersion along the highly symmetric path Γ -K-M- Γ in the right figure clearly indicates that the valence band and conduction band intersect linearly near point *K* in **Figure 5(b)**, verifying the existence of Dirac cones. The linear dispersion relationship indicates that the quasi particles excited by graphene at low energy follow the massless Dirac equation, with a Fermi velocity of approximately 1.0×10^6 m/s. The symmetric distribution of Dirac points in the band structure is a typical characteristic of graphene as a topological semimetal.

Our derivation further elucidates that at another non equivalent Dirac point (K' point), the low-energy effective Hamiltonian and wave function can be expressed as:

$$\hat{H}_{K'}(\mathbf{q}) \approx \hbar v_F (-\sigma_x q_x + \sigma_y q_y), \quad \psi_{\lambda, K'}(\mathbf{q}) = \frac{1}{\sqrt{2}} \begin{pmatrix} 1 \\ -\lambda e^{-i\phi_q} \end{pmatrix} \quad (3)$$

Compared with the point, its helical phase has opposite chirality ($e^{-i\phi_q}$), topological charge is -1, and the vortex direction of the pseudo spin texture is also opposite. The K point and K' point together constitute the Valley Degree of Freedom of graphene, and these two valleys are interrelated under time reversal symmetry. The opposite chirality between valleys lays the theoretical foundation for selectively manipulating electrons in specific valleys through electric fields, strain, or boundary control, known as "valley electronics" research.

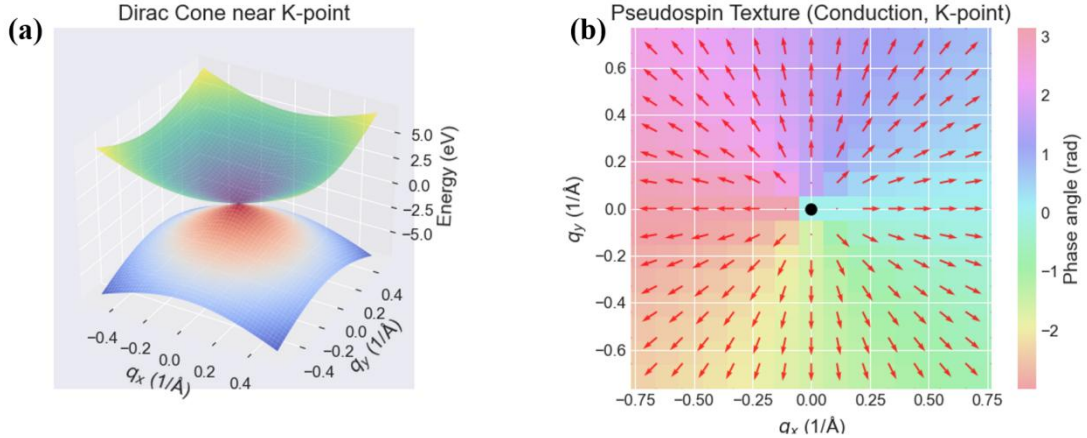


Figure 6: (a) Dirac cone near point K on a three-dimensional surface; (b) Pseudo spin texture in momentum space

Figure 6(a) depicts the Dirac cone near point K in three-dimensional curved form, visually demonstrating the linear dependence of energy and momentum, and the cone surface is symmetrical vertically. **Figure 6(b)** shows the pseudospin texture in momentum space: the direction of the arrow represents the expected direction of pseudospin (pseudovector of subgrid degrees of freedom) in the conduction band. It can be seen that the pseudo spin is completely locked in the direction of momentum - on any circumference around the Dirac point, the pseudo spin is arranged along the tangential direction, forming a planar vortex. This texture directly corresponds to the phase factor $e^{i\phi_q}$ of the spiral wave function, which is a visual manifestation of the chirality of graphene electrons.

A direct and significant consequence of the spiral wave function is the generation of non-zero Berry phases. When electrons undergo adiabatic evolution along a closed path around the Dirac point in momentum space, their wave function accumulates a Berry phase γ determined by the system geometry in addition to the dynamic phase. For the above wave function, $\gamma = \pi$ can be calculated.

This Berry phase is a key indicator of the non mediocrity of graphene band topology. It profoundly affects the quantum transport behavior of graphene:

1. Half integer quantum Hall effect: Under strong magnetic fields, traditional two-dimensional electron gases exhibit integer quantum Hall effect. Due to the existence of the π Berry phase in graphene, the degeneracy and sequence of its Landau energy levels change, ultimately leading to the appearance of quantum Hall platforms at fill factors of $v = \pm 2, \pm 6, \pm 10, \dots$, where the platform at $v = \pm 2$ is a characteristic manifestation of its "semi integer" shift.

2. Suppression of weak anti localization: In disordered systems, the π Berry phase will cause the quantum interference of time reversal path pairs to shift from

destructive (weak localization) to constructive (weak anti localization), resulting in a characteristic positive magnetic resistance signal in low magnetic field magnetoresistance. This theory is perfectly consistent with experimental observations.

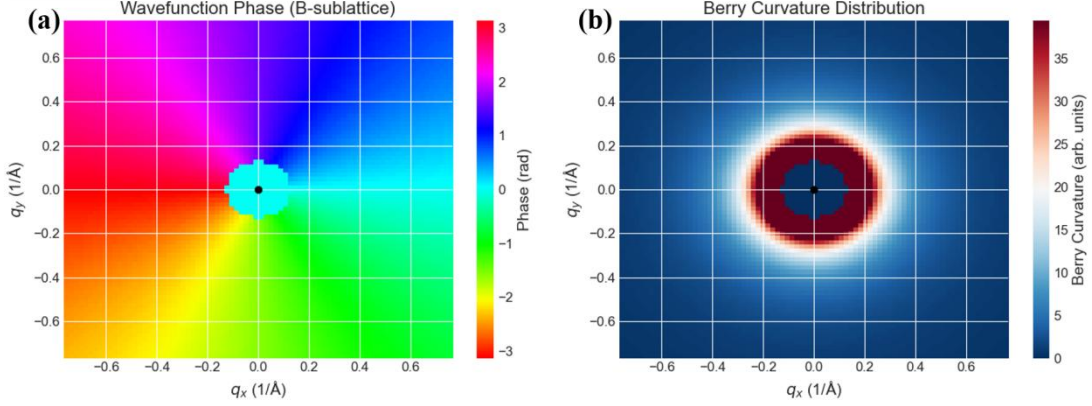


Figure 7: (a) Phase distribution of the conduction band electron wave function on the B lattice component; (b) Distribution of Berry curvature in momentum space

Figure 7(a) shows the phase distribution of the conduction band electron wave function on the B lattice component. The color change represents the phase value (- π to π), and it can be clearly observed that the phase continuously changes around the Dirac point, completing one 2π orbit. This phase vortex has an integer winding number (winding number+1), which is direct evidence of the non trivial topological structure of the wave function. The phase singularity is located at the Dirac point, where the corresponding wave function is undefined, resulting in the particularity of the zero energy state. This vortex structure is the geometric origin of the π Berry phase.

Figure 7(b) shows the distribution of Berry curvature in momentum space. The Berry curvature exhibits a sharp peak near the Dirac point and rapidly decays with increasing distance. Its sign is opposite at points K and K' , reflecting the valley degrees of freedom brought about by time reversal symmetry. This curvature distribution indicates that electrons undergo non trivial geometric phase accumulation in momentum space; Following a closed path adiabatic motion around the Dirac point for one revolution will result in a Berry phase of π . This topological phase directly leads to the appearance of a semi integer quantization plateau ($\sigma_{xy}=\pm 4e^2/h(n+1/2)$) in graphene quantum Hall conductance, which is different from traditional two-dimensional electron gases.

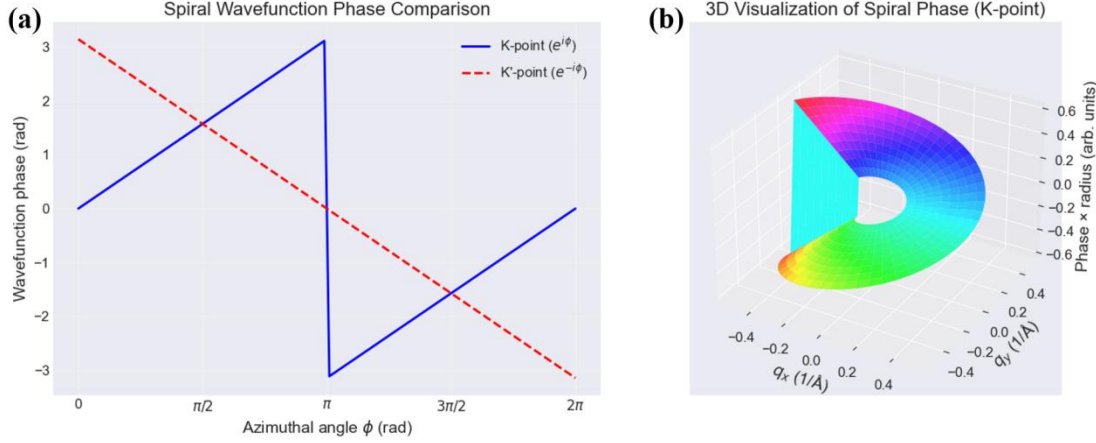


Figure 8: (a) Phase variation of wave functions at point K and K' with respect to azimuth angle; (b) 3D Spiral Phase

Figure 8(a) compares the phase variation of the wave functions at point K and point K' with respect to azimuth angle. The phase of the conduction band wave function at point K increases linearly with ϕ ($e^{i\phi_q}$), while at point K' it decreases linearly ($e^{-i\phi_q}$), indicating that the two valleys have opposite chirality. This valley dependent spiral structure leads to pseudo spin and momentum direction locking of electrons during transport, which strongly suppresses backscattering and is an important mechanism for the high mobility of graphene. The 3D spiral phase visualization in Figure 8b further highlights the continuous spiral structure of phase in momentum space.

The low-energy effective wave function of graphene can be expressed as $\Psi(q) = 1/\sqrt{2} \begin{pmatrix} 1, e^{i\phi_q} \end{pmatrix}^T$, where the phase factor $e^{i\phi_q}$ reflects the helical nature of the wave function. This mathematical form directly leads to: 1) pseudo spin and momentum locking; 2) Momentum space phase vortex; 3) π Berry phase; 4) Valley degree of freedom. These topological characteristics collectively contribute to the unique transport behavior of graphene, such as weak anti localization loss, minimum conductivity plateau, and room temperature quantum Hall effect. The concept of spiral wave function is not only applicable to graphene, but also provides a universal framework for understanding other Dirac materials, such as topological insulating surface states.

In summary, we have demonstrated through systematic deduction that the low-energy quasi particle state of graphene can be described by a wave function with spiral vortex characteristics. This wave function originates from the symmetry of graphene honeycomb lattice, which directly gives rise to a series of topological non trivial properties such as pseudo spin momentum locking, π Berry phase, and valley chirality. These properties together constitute the microscopic physical mechanism of graphene's

peculiar electron transport behavior. This study not only solidifies the fundamental understanding of graphene as a prototype Dirac material, but its core theoretical paradigm - wave functions with vortex textures in momentum space and their related topological invariants - has been widely extended to the entire field of topological materials. For example, wave functions with similar structures can be observed near the intersection of the surface states of topological insulators and the energy bands of topological semimetals. In the future, coherent manipulation based on such spiral wave functions is expected to open up new research directions in topological quantum computing, low-power electronics, and novel spin valley electronic devices.

4. Conclusion

This study employs the BBC and an improved BBC model to systematically investigate graphene's electronic structure, elucidating the electrostatic screening effect, evolution of band structure and density of states (DOS), and topologically non-trivial properties. The key conclusions are:

1. The screening parameter σ_v quantitatively tunes electrostatic interactions. The BBC potential effectively suppresses electron-electron interactions. In the improved model, the hopping integral decays with distance and is sensitive to σ_v , while the on-site energy increases weakly with σ_v . Both models eliminate the Coulomb singularity, with hopping integrals vanishing at long range.

2. σ_v directs band renormalization: energies at high-symmetry points decrease with σ_v in the BBC model, while showing opposite trends at Γ and K in the improved model, indicating momentum selectivity. Band narrowing occurs, and a bandgap may open for $\sigma_v \geq 1.00$. The DOS peaks at the Fermi level, with the high-energy region slightly increasing with σ_v .

3. Graphene's low-energy states are described by helical wavefunctions, yielding topological properties like pseudospin-momentum locking and a π Berry phase, which explain unique transport phenomena. This "wavefunction-topology" framework is broadly applicable.

This work establishes screening principles and validates the helical wavefunction description, supporting research into 2D material topology. Tuning σ_v via gating or substrates allows continuous electronic parameter adjustment for device design. Future work should quantify σ_v 's net effect on on-site energy, conduct experimental validation (e.g., STS, XPS), and explore device concepts based on wavefunction engineering.

Acknowledgement

This study was financially supported by four research programs: 1) the Science and Technology Research Project of Fuling District, Chongqing Municipality (Grant No. FLKJ-2024BAG5128); 2) the Science and Technology Research Program of Chongqing Municipal Education Commission (Grant No. KJZD-K202501406); 3) Program of the Chongqing Municipal Education Commission (Grant No. KJQN-202401420); 4) the Science and Technology Research Project of Fuling District, Chongqing Municipality (Grant No. FLKJ-2024BAG5133)

References:

- [1] A. K. Geim *science*. **2009**, 324, 1530-1534.
- [2] A. K. Geim, K. S. Novoselov *Nature materials*. **2007**, 6, 183-191.
- [3] T. Ramachandran, N. Roy, H. Hegazy, I. Yahia, Y. A. Kumar, M. Moniruzzaman, S. W. Joo *Journal of Alloys and Compounds*. **2025**, 1010, 177248.
- [4] B. Xie, Y. Guo, Y. Chen, H. Zhang, J. Xiao, M. Hou, H. Liu, L. Ma, X. Chen, C. Wong *Nano-Micro Letters*. **2025**, 17, 17.
- [5] D. Hua, Q. Xia, J. Li, Q. Zhou, M. Xie, S. Liu, S. J. Eder, H. Wang *Acta Materialia*. **2025**, 287, 120809.
- [6] T. Han, Z. Lu, Z. Hadjri, L. Shi, Z. Wu, W. Xu, Y. Yao, A. A. Cotten, O. Sharifi Sedeh, H. Weldeyesus *Nature*. **2025**, 643, 654-661.
- [7] B. Gao, X. Feng, Y. Zhang, Z. Zhou, J. Wei, R. Qiao, F. Bi, N. Liu, X. Zhang *Chemical Engineering Journal*. **2024**, 484, 149604.
- [8] A. Kahn *Materials Horizons*. **2016**, 3, 7-10.
- [9] A. N. Grigorenko, M. Polini, K. S. Novoselov *Nature photonics*. **2012**, 6, 749-758.
- [10] I. Meric, M. Y. Han, A. F. Young, B. Ozyilmaz, P. Kim, K. L. Shepard *Nature nanotechnology*. **2008**, 3, 654-659.
- [11] D. Zhan, J. Yan, L. Lai, Z. Ni, L. Liu, Z. Shen *Advanced Materials*. **2012**, 24, 4055-4069.
- [12] M. Liu, X. Yin, E. Ulin-Avila, B. Geng, T. Zentgraf, L. Ju, F. Wang, X. Zhang *Nature*. **2011**, 474, 64-67.
- [13] S. Schulz, G. Czycholl *Physical Review B—Condensed Matter and*

Materials Physics. **2005**, *72*, 165317.

- [14] X. Kuang, F. Escudero, P. A. Pantaleón, F. Guinea, Z. Zhan *Physical Chemistry Chemical Physics.* **2025**.
- [15] S. Javvaji, F. Li, J. Jung *Physical Review Materials.* **2025**, *9*, 024004.
- [16] M. R. Maamoon, A. Khalaf, M. Kotb, M. Sadeq, M. A. Kher-Elden, I. Piquero-Zulaica, Z. M. A. El-Fattah *Scientific Reports.* **2025**, *15*, 19218.
- [17] M. Bo, H. Li, Z. Wang, Y. Zhong, Y. Chuang, Z. Huang *Physica B: Condensed Matter.* **2023**, *652*, 414624.
- [18] Y. Wang, Y. Zhu, Y. Li, M. Bo *physica status solidi (b).* **2025**, *262*, 2400664.
- [19] Y.-W. Liu, Y.-C. Zhuang, Y.-N. Ren, C. Yan, X.-F. Zhou, Q. Yang, Q.-F. Sun, L. He *Nature Communications.* **2024**, *15*, 3546.
- [20] M. Wimmer, H. M. Price, I. Carusotto, U. Peschel *Nature Physics.* **2017**, *13*, 545-550.
- [21] P. Gosselin, A. Bérard, H. Mohrbach, S. Ghosh *The European Physical Journal C.* **2009**, *59*, 883-889.
- [22] Y. Shimazaki, M. Yamamoto, I. V. Borzenets, K. Watanabe, T. Taniguchi, S. Tarucha *Nature Physics.* **2015**, *11*, 1032-1036.
- [23] L. Ge, M. Bo *Physica Scripta.* **2023**, *98*, 105908.
- [24] Y. Tan, M. Bo *Results in Chemistry.* **2025**, 102635.
- [25] Y. Zhang, Y. Su, L. He *Physical Review Letters.* **2020**, *125*, 116804.
- [26] Y. Zhang, Y. Su, L. He *Nano Letters.* **2021**, *21*, 2526-2531.